

# ICES REPORT 09-05

---

February 2009

## **Isogeometric Shell Analysis: The Reissner-Mindlin Shell**

by

D.J. Benson, Y. Bazilevs, M.C. Hsu, And T.J.R.  
Hughes



**The Institute for Computational Engineering and Sciences**  
The University of Texas at Austin  
Austin, Texas 78712

# Isogeometric Shell Analysis: The Reissner-Mindlin Shell

D.J. Benson <sup>a,1</sup>, Y. Bazilevs <sup>a,2</sup>, M.C. Hsu <sup>a,3</sup>, and T.J.R. Hughes <sup>b,4</sup>

<sup>a</sup>*Department of Structural Engineering, University of California, San Diego 9500 Gilman Drive, La Jolla, CA 92093, USA*

<sup>b</sup>*Institute for Computational Engineering and Sciences, The University of Texas at Austin, 201 East 24th Street, 1 University Station C0200, Austin, TX 78712, USA*

---

## Abstract

A Reissner-Mindlin shell formulation based on a degenerated solid is implemented for NURBS-based isogeometric analysis. The performance of the approach is examined on a set of linear elastic and nonlinear elasto-plastic benchmark examples. The analyses were performed with LS-DYNA, an industrial, general-purpose finite element code, for which a user-defined shell element capability was implemented. This new feature, to be reported on in subsequent work, allows for the use of NURBS and other non-standard discretizations in a sophisticated nonlinear analysis framework.

*Key words:* isogeometric analysis, NURBS, shells, user-defined elements

---

---

<sup>1</sup> Professor

<sup>2</sup> Assistant Professor

<sup>3</sup> Graduate Research Assistant

<sup>4</sup> Professor of Aerospace Engineering and Engineering Mechanics, Computational and Applied Mathematics Chair III

## Contents

1	Introduction	2
2	NURBS-based isogeometric analysis fundamentals	4
3	The Reissner-Mindlin shell formulation	6
3.1	The principle of virtual power	6
3.2	Shell kinematics	6
3.3	Departures from the standard formulation	7
3.4	Discrete gradient operator	8
3.5	Definition of the local coordinate system	9
3.6	Stress update in the co-rotational formulation	10
3.7	Evaluation of the residual, the stiffness matrix, and the rotational stiffnesses	10
3.8	Mass matrix	11
3.9	Boundary conditions	11
3.10	Time step size estimation	12
4	Numerical Examples	14
4.1	Linear elastic benchmark example – Pinched cylinder	14
4.2	Nonlinear elasto-plastic examples	16
5	Conclusions	25

## 1 Introduction

Isogeometric analysis is a new computational method that is based on geometry representations (i.e. basis functions) developed in computer-aided design (CAD), computer graphics (CG), and animation, with a far-reaching goal to bridge the existing gap between CAD and analysis [29]. For the first instantiation of the isogeometric methodology, non-uniform rational B-splines (NURBS) were chosen as a basis, due to their relative simplicity and ubiquity in the worlds of CAD, CG, and

animation. It was found that not only are NURBS applicable to engineering analysis, in many cases they were better suited for the application at hand, and were able to deliver accuracy superior to standard finite elements (see, e.g., [1, 2, 4–6, 19, 30, 40]). Subdivision surfaces [15–17] and, more recently, T-Splines [3, 20], were also successfully employed in the analysis context.

CAD, CG and animation make use of boundary or surface representations to model geometrical objects, while analysis often requires a full volumetric description of the geometry. This makes integration of design and analysis a complicated task because no well-established techniques exist that allow one to go from a boundary to a volumetric representation in a fully automated way. A polycube spline technique developed by Wang *et al.* [41] constitutes a promising solution to this problem.

A well-developed branch of computational engineering, with a wide range of industrial applications, that does not require a volumetric description of the underlying geometry is shell analysis. As a result, bridging design and shell analysis does not constitute such a daunting task. Provided that the geometry surface description makes use of basis functions with good approximation properties, and that they are conforming to a given function space, one may, in principle, perform shell analyses directly off of CAD data. Unfortunately, most CAD descriptions make use of the trimmed surface technology, which is not directly applicable to analysis. Höllig and co-workers developed the concept of web splines, based on appropriate boundary weighting functions, to address the issue of trimmed surfaces in the B-Spline finite element method [25]. Although good computational performance was achieved on a set of benchmark problems, this technique appears somewhat cumbersome for real-life applications. An alternative solution to the trimmed surface problem was recently proposed by Sederberg *et al.* [38] in which a trimmed spline surface is replaced by a locally refined T-Spline representation. The latter, in principle, leads to an explicit, analysis-suitable discretization of the resulting surface, and, in our opinion, constitutes a solution to the trimmed surface problem that can be applied to problems of engineering interest. Of course, numerical evidence and mathematical theory must be provided in support of this claim.

The shell formulation presented here was implemented using the LS-DYNA user-defined elements. The elements, which may have an arbitrary number of nodes, are defined entirely in the input file by the integration rule and the values of the basis functions and their derivatives at the integration points. This capability was developed to facilitate the rapid prototyping of elements without programming, and therefore the execution speed is much less than the standard elements within the LS-DYNA. A detailed description will be provided in a future article.

The paper is outlined as follows. In Section 2 we give a brief review of isogeometric analysis based on NURBS. In Section 3 we describe the details of the Reissner-Mindlin shell formulation. In Section 4 we solve a linear benchmark problem from the shell obstacle course, the pinched cylinder. In Section 5 we present computa-

tional results for several nonlinear elastic-plastic cases. We draw conclusions and outline current and future research directions in Section 6.

## 2 NURBS-based isogeometric analysis fundamentals

Non-Uniform Rational B-Splines (NURBS) are a standard tool for describing and modeling curves and surfaces in computer aided design and computer graphics (see, e.g., Piegl and Tiller [35], Rogers [36], and Cohen, Riesenfeld and Elber [18]). The aim of this section is to introduce them briefly and to present an overview of isogeometric analysis, for which an extensive account has been given in Hughes, Cottrell and Bazilevs [29].

B-splines are piecewise polynomial curves composed of linear combinations of B-spline basis functions. The coefficients are points in space, referred to as control points. A knot vector,  $\Xi$ , is a set of non-decreasing real numbers representing coordinates in the parametric space of the curve:

$$\Xi = \{\xi_1, \xi_2, \dots, \xi_{n+p+1}\}, \quad (1)$$

where  $p$  is the order of the B-spline and  $n$  is the number of basis functions (and control points) necessary to describe it. The interval  $[\xi_1, \xi_{n+p+1}]$  is called a patch.

Given a knot vector,  $\Xi$ , B-spline basis functions are defined recursively starting with  $p = 0$  (piecewise constants):

$$N_{i,0}(\xi) = \begin{cases} 1 & \text{if } \xi_i \leq \xi < \xi_{i+1}, \\ 0 & \text{otherwise.} \end{cases} \quad (2)$$

For  $p = 1, 2, 3, \dots$ , the basis is defined by the following recursion formula:

$$N_{i,p}(\xi) = \frac{\xi - \xi_i}{\xi_{i+p} - \xi_i} N_{i,p-1}(\xi) + \frac{\xi_{i+p+1} - \xi}{\xi_{i+p+1} - \xi_{i+1}} N_{i+1,p-1}(\xi). \quad (3)$$

Using tensor products, B-spline surfaces can be constructed starting from knot vectors  $\Xi = \{\xi_1, \xi_2, \dots, \xi_{n+p+1}\}$  and  $\mathcal{H} = \{\eta_1, \eta_2, \dots, \eta_{m+q+1}\}$ , and an  $n \times m$  net of control points  $\mathbf{x}_{i,j}$ , also called the *control mesh*. One-dimensional basis functions  $N_{i,p}$  and  $M_{j,q}$  (with  $i = 1, \dots, n$  and  $j = 1, \dots, m$ ) of order  $p$  and  $q$ , respectively, are defined from the corresponding knot vectors, and the B-spline surface is constructed as:

$$S(\xi, \eta) = \sum_{i=1}^n \sum_{j=1}^m N_{i,p}(\xi) M_{j,q}(\eta) \mathbf{x}_{i,j}. \quad (4)$$

The patch for the surface is now the domain  $[\xi_1, \xi_{n+p+1}] \times [\eta_1, \eta_{m+q+1}]$ . Identifying the logical coordinates  $(i, j)$  of the B-spline surface with the traditional notation of a node,  $A$ , and the Cartesian product of the associated basis functions with the shape function,  $N_A(\xi, \eta) = N_{i,p}(\xi)M_{j,q}(\eta)$ , the familiar finite element notation is recovered, namely,

$$S(\xi, \eta) = \sum_{A=1}^{nm} N_A(\xi, \eta) \mathbf{x}_A. \quad (5)$$

Non-uniform rational B-splines (NURBS) are obtained by augmenting every point in the control mesh  $\mathbf{x}_A$  with the homogenous coordinate  $w_A$ , then dividing the expression (5) through by the weighting function,  $w(\xi, \eta) = \sum_{A=1}^{nm} N_A(\xi, \eta) w_A$ , giving the final spatial surface definition,

$$S(\xi, \eta) = \frac{\sum_{A=1}^{nm} N_A(\xi, \eta) w_A \mathbf{x}_A}{w(\xi, \eta)} = \sum_{A=1}^{nm} \bar{N}_A(\xi, \eta) \mathbf{x}_A. \quad (6)$$

In equation (6),  $\bar{N}_A(\xi, \eta) = N_A(\xi, \eta)/w(\xi, \eta)$ , are the rational basis functions. These functions are pushed forward by the surface mapping  $S(\xi, \eta)$  in (6) to form the approximation space for NURBS-based shell analysis. Note that  $w_A$ 's are not treated as solution variables, they are data coming from the description of the NURBS surface. In Figure 1 we present an example consisting of a  $6 \times 6$  quadratic NURBS mesh of a quarter hemisphere and selected corner, edge, and interior NURBS basis functions defined on the actual geometry.

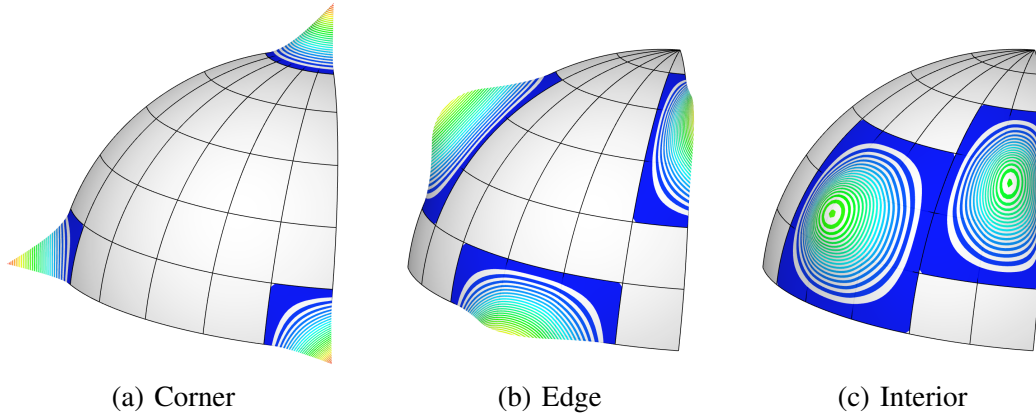


Fig. 1. NURBS mesh of a quarter hemisphere consisting of  $6 \times 6$  quadratic elements. Selected corner, edge, and interior basis functions are plotted on the actual geometry, which is represented exactly.

In the remainder of the paper, we will suppress the superposed bar on the rational basis functions.

### 3 The Reissner-Mindlin shell formulation

The primary applications for the shell element involve large deformation plasticity, and therefore it is formulated using an updated Lagrangian approach. Although the increased continuity ( $C^1$  or higher) of the NURBS basis functions permits a Kirchhoff-Love formulation, a Reissner-Mindlin formulation, for which a  $C^0$ -continuous discretization is sufficient for well-posedness, is used here because it is more appropriate for metal forming applications that often involve sharp creases in both the initial geometry and solution. For an excellent review of shell theories and numerical formulations see Bischoff *et al.* [14].

#### 3.1 The principle of virtual power

The starting point is the principle of virtual power in three dimensions,

$$\int_V \rho \mathbf{a} \delta \mathbf{v} + \boldsymbol{\sigma} : \delta \mathbf{D} dV = \int_{\Gamma} \mathbf{t} \delta \mathbf{v} d\Gamma + \int_V \mathbf{b} \delta \mathbf{v} dV \quad (7)$$

where  $\rho$  is the density,  $\mathbf{a}$  is the acceleration,  $\boldsymbol{\sigma}$  is the Cauchy stress,  $\mathbf{t}$  is the traction,  $\mathbf{b}$  is the body force, and  $V$  and  $\Gamma$  are the volume and the appropriate surface area, respectively. On the boundary  $\Gamma_{v_i}$ , the velocity component  $v_i$  is specified, and the virtual velocity component  $\delta v_i$  is zero. The virtual rate of deformation,  $\delta \mathbf{D}$ , is defined as

$$\delta \mathbf{L} = \frac{\partial \delta \mathbf{v}}{\partial \mathbf{x}}, \quad \delta \mathbf{D} = \frac{1}{2} (\delta \mathbf{L} + \delta \mathbf{L}^T). \quad (8)$$

#### 3.2 Shell kinematics

The shell kinematics are based on the degenerated solid element approach developed by Hughes and Liu [27]. They are derived by starting with a solid element that has linear interpolation through the thickness coupled with the desired form of interpolation on the laminae. Pairs of control points on the upper and lower surfaces define a material fiber,  $\mathbf{y}$ , that remains straight during the deformation. The motion of the fiber is therefore a rigid body motion (although this contradicts the zero normal stress condition) that may be described in terms of three translational velocities and either two or three rotational velocities (the rotation about the axis of the fiber does not contribute to the deformation but it is simpler computationally to use three angular velocities in the global coordinate system).

The kinematics are therefore reduced to approximating a shell by a surface in space defined by the translational coordinates of a set of nodes, and the rotation of the fiber vectors attached to them. The current shell geometry is therefore expressed

mathematically by

$$\mathbf{x}(\boldsymbol{\xi}) = \sum_A N_A(\boldsymbol{\xi}, \eta) \left( \mathbf{x}_A + \frac{h_A}{2} \zeta \hat{\mathbf{y}}_A \right) \quad (9)$$

where  $\mathbf{x}$  is the current coordinate vector,  $\boldsymbol{\xi}$  is the vector of parametric coordinates  $(\xi, \eta, \zeta)$ ,  $h$  is the thickness, and  $\hat{\mathbf{y}}$  is the unit fiber vector. The coordinates  $\xi$  and  $\eta$  are from the parametric space, and therefore their ranges are defined by the appropriate knot vectors, and the third coordinate,  $\zeta \in [-1, +1]$ , is used with the standard linear interpolation functions through the thickness of the shell.

To simplify the notation, the dependence of the functions on the parametric coordinates is dropped, however, all are assumed to be evaluated at the integration point under consideration. Additionally, since the product of  $N_A$  and  $\zeta$  appears throughout the terms associated with the rotational degrees of freedom, the additional functions  $\hat{N}_A = N_A \zeta$  are introduced. For example, the expression for the current geometry is now written as

$$\mathbf{x} = \sum_A N_A \mathbf{x}_A + \frac{h_A}{2} \hat{N}_A \hat{\mathbf{y}}_A \quad (10)$$

and the resulting Jacobian,  $\mathbf{J}$ , is therefore

$$\mathbf{J} = \frac{\partial \mathbf{x}}{\partial \boldsymbol{\xi}} = \sum_A \frac{\partial N_A}{\partial \boldsymbol{\xi}} \mathbf{x}_A + \frac{h_A}{2} \frac{\partial \hat{N}_A}{\partial \boldsymbol{\xi}} \hat{\mathbf{y}}_A. \quad (11)$$

The velocity,  $\mathbf{v}$ , is defined in terms of the translational velocity,  $\mathbf{v}_A$ , and the angular velocity,  $\boldsymbol{\omega}_A$ , of the control points, both in the global coordinate system,

$$\mathbf{v} = \sum_A N_A \mathbf{v}_A + \frac{h_A}{2} \hat{N}_A \boldsymbol{\omega}_A \times \hat{\mathbf{y}}_A. \quad (12)$$

This choice is motivated by the simplicity of joining multiple non-smooth surfaces (e.g., a honeycomb structure). Using three rotational degrees of freedom introduces a singularity associated with the rotation about  $\hat{\mathbf{y}}$  for smooth surfaces, which we address later. The test space, or virtual velocity,  $\delta \mathbf{v}$  has the same structure as the velocity field,

$$\delta \mathbf{v} = \sum_A N_A \delta \mathbf{v}_A + \frac{h_A}{2} \hat{N}_A \delta \boldsymbol{\omega}_A \times \hat{\mathbf{y}}_A. \quad (13)$$

### 3.3 Departures from the standard formulation

The basic degenerated solid formulation is modified in three ways, motivated by Belytshcko *et al.* [8, 9]. First,  $\hat{\mathbf{y}}$  is replaced by  $\mathbf{n}$ , the unit normal in the shell laminae, throughout. The motivation for this simplification is to alleviate the artificial thinning that sometimes occurs with explicit time integration, which is caused by

the scaling of the rotational inertias to maintain a large time step size. Additionally, the definition of a unique fiber direction for structures with intersecting shell surfaces is often problematical.

Second, in contrast to the standard formulations, which are focused on elements with linear basis functions, nothing is done to alleviate shear locking in the current formulation because we are interested in the higher order NURBS basis functions where shear locking is generally not a problem. For lower degree NURBS, the generalization of  $\bar{\mathbf{B}}$  for volumetric locking developed for isogeometric elements [21] may be modified for shear locking.

Finally, a corotational formulation [9] for the stress is used here instead of the Truesdell rate originally used by Hughes and Liu [27]. This choice was motivated by our desire to use the isogeometric shells for metal forming, where the corotational formulation has been found to provide extra robustness.

### 3.4 Discrete gradient operator

The spatial velocity gradient,  $\mathbf{L}^g$ , and spatial virtual velocity gradient,  $\delta\mathbf{L}^g$ , in global coordinates, are given by

$$\mathbf{L}^g = \frac{\partial \mathbf{v}}{\partial \mathbf{x}} = \sum_A \frac{\partial N_A}{\partial \mathbf{x}} \mathbf{v}_A + \frac{h_A}{2} \frac{\partial \hat{N}_A}{\partial \mathbf{x}} \boldsymbol{\omega}_A \times \hat{\mathbf{y}}_A \quad (14)$$

$$\delta\mathbf{L}^g = \frac{\partial \delta \mathbf{v}}{\partial \mathbf{x}} = \sum_A \frac{\partial N_A}{\partial \mathbf{x}} \delta \mathbf{v}_A + \frac{h_A}{2} \frac{\partial \hat{N}_A}{\partial \mathbf{x}} \delta \boldsymbol{\omega}_A \times \hat{\mathbf{y}}_A \quad (15)$$

and the corresponding rates of deformation,  $\mathbf{D}^g$  and  $\delta\mathbf{D}^g$ , are

$$\mathbf{D}^g = \frac{1}{2} [\mathbf{L}^g + (\mathbf{L}^g)^T] \quad \text{and} \quad \delta\mathbf{D}^g = \frac{1}{2} [\delta\mathbf{L}^g + (\delta\mathbf{L}^g)^T]. \quad (16)$$

The  $\mathbf{B}$  matrix is defined by

$$\mathbf{D}^g = \mathbf{B} \mathbf{v} \quad \text{and} \quad \delta\mathbf{D}^g = \mathbf{B} \delta \mathbf{v} \quad (17)$$

where  $\mathbf{D}^g$  is the strain rate vector obtained using Voigt notation,

$$\mathbf{D}^g = \{D_{11}^g \ D_{22}^g \ D_{33}^g \ 2D_{12}^g \ 2D_{23}^g \ 2D_{31}^g\} \quad (18)$$

and  $\mathbf{v}$  is the generalized velocity vector,

$$\mathbf{v} = \{\dots, v_{A1}, v_{A2}, v_{A3}, \omega_{A1}, \omega_{A2}, \omega_{A3}, \dots\}. \quad (19)$$

The contribution of control point  $A$  to  $\mathbf{B} = [\mathbf{B}_1 \dots \mathbf{B}_A \dots \mathbf{B}_n]$  is

$$\mathbf{B}_A = [\mathbf{B}_A^v, \mathbf{B}_A^\omega] \quad (20)$$



the remaining local coordinate vectors are

$$\mathbf{e}_1^\ell = \frac{\sqrt{2}}{2} (\mathbf{t}_\alpha - \mathbf{t}_\beta), \quad (28)$$

$$\mathbf{e}_2^\ell = \frac{\sqrt{2}}{2} (\mathbf{t}_\alpha + \mathbf{t}_\beta). \quad (29)$$

The rotation matrix from the local to the global coordinate system,  $\mathbf{v}^g = \mathbf{R}\mathbf{v}^\ell$ , is

$$\mathbf{R} = \begin{bmatrix} \mathbf{e}_1^\ell & \mathbf{e}_2^\ell & \mathbf{e}_3^\ell \end{bmatrix}. \quad (30)$$

### 3.6 Stress update in the co-rotational formulation

The stress is updated in the local coordinate system using the local rate of deformation,  $\mathbf{D}^\ell$ ,

$$\mathbf{D}^\ell = \mathbf{R}^T \mathbf{D}^g \mathbf{R} \quad (31)$$

The normal component,  $D_{33}^\ell$ , is calculated within the constitutive model to satisfy the zero normal stress condition  $\sigma_{33}^\ell = 0$ . The algorithm for calculating  $D_{33}^\ell$  depends on the particular constitutive model [24, 37, 39]. The updated stress is rotated into the global coordinate system at the end of the time step for evaluating the residual,

$$\boldsymbol{\sigma} = \mathbf{R} \boldsymbol{\sigma}^\ell \mathbf{R}^T. \quad (32)$$

### 3.7 Evaluation of the residual, the stiffness matrix, and the rotational stiffnesses

The integration of the residual and the stiffness matrix are performed using the standard tensor product of one-dimensional Gauss quadrature rules over the lamina and through the thickness [26]. The parametric domain for an element over the lamina is  $[\xi_i, \xi_{i+1}] \times [\eta_j, \eta_{j+1}]$ , the product of adjacent pairs of knots in each parametric direction. Note that repeated knots routinely occur in the knot vector definitions for B-Splines and NURBS, introducing elements with zero area that are skipped within the element evaluation loop.

The residual contribution from the stress is

$$\mathbf{F} = \begin{Bmatrix} \mathbf{F}^v \\ \mathbf{F}^\omega \end{Bmatrix} = - \int_V \begin{bmatrix} (\mathbf{B}^v)^T \\ (\mathbf{B}^\omega)^T \end{bmatrix} \boldsymbol{\sigma} dV. \quad (33)$$

where the stress tensor has been reduced to a vector using Voigt notation,  $\boldsymbol{\sigma} = \{\sigma_{11}, \sigma_{22}, \sigma_{33}, \sigma_{12}, \sigma_{23}, \sigma_{31}\}^T$ .

The material tangent contribution to the stiffness matrix is

$$\mathbf{K} = \begin{bmatrix} \mathbf{K}^{vv} & \mathbf{K}^{v\omega} \\ \mathbf{K}^{\omega v} & \mathbf{K}^{\omega\omega} \end{bmatrix} = \int_V \begin{bmatrix} (\mathbf{B}^v)^T \\ (\mathbf{B}^\omega)^T \end{bmatrix} \mathbf{C} \begin{bmatrix} \mathbf{B}^v & \mathbf{B}^\omega \end{bmatrix} dV \quad (34)$$

where  $\mathbf{C}$  is the material tangent matrix.

The singularity of the stiffness matrix associated with the rotations about the normal direction at the control points is addressed by adding a small rotational stiffness in the normal direction on a control point-by-control point basis,

$$\mathbf{K}_{AA}^{\omega\omega} \leftarrow \mathbf{K}_{AA}^{\omega\omega} + sk\mathbf{n}_A \otimes \mathbf{n}_A, \quad (35)$$

where  $\mathbf{K}_{AA}^{\omega\omega}$  is the  $3 \times 3$  diagonal sub-matrix associated with control point  $A$ ,  $s$  is a small number on the order of  $10^{-4} \sim 10^{-6}$ ,  $k$  is the maximum value along the sub-matrix diagonal, and  $\mathbf{n}_A$  is the normal for node  $A$ . This procedure was adopted during the current research for expediency, and because it has been successfully used in LS-DYNA for many years for some of its shell elements. The formulation of the geometric stiffness is omitted because the only implicit problem considered later is linearly elastic; all the large deformation calculations are explicit.

### 3.8 Mass matrix

A lumped mass based on row summing is used with the explicit formulation. The translational mass for node  $A$  contributed by an element is

$$M_A = \int_V \rho N_A dV = h \int_A \rho N_A dA \quad (36)$$

where  $dV = h dA$ , where  $dA$  is the differential area on the reference lamina. The rotational inertia is

$$J_A = \alpha \frac{h^3}{12} \int_A \rho N_A dA = \alpha \frac{h^2}{12} M_A \quad (37)$$

where  $\alpha$  is chosen so that the time step is not controlled by the rotational inertia [26]. Note that, due to the pointwise positivity of NURBS,  $N_A$ , and consequently  $M_A$ , is guaranteed to be positive. More sophisticated lumping schemes [26] have been tested, but there was no significant difference between them for the problems presented later in this paper.

### 3.9 Boundary conditions

Distributed boundary conditions, such as contact and pressure loads, are currently handled in an approximate manner. Each isogeometric element is uniformly sub-

divided in the parametric coordinate system into a patch of  $n \times n$  interpolation quadrilateral elements defined by  $(n + 1)^2$  nodes that are interpolated from the isogeometric element geometry,

$$\mathbf{x}_B^I = \sum_A N_A(\xi_B, \eta_B) \mathbf{x}_A \quad (38)$$

where the superscript  $I$  indicates a variable associated with an interpolation node. After the distributed loads are evaluated for interpolated nodes and elements using the standard routines within LS-DYNA, the control point forces are evaluated

$$\mathbf{F}_A = \sum_{B=1}^{NIN} N_A(\xi_B, \eta_B) \mathbf{F}_B^I \quad (39)$$

where  $NIN$  is the number of interpolated nodes.

The accuracy of this approximation of the distributed loading is clearly a function of the number of interpolation elements used to approximate the isogeometric element geometry. In the example calculations, the number of elements in each direction is equal to order of the interpolation,  $p$ . A quadratic isogeometric element is divided into four interpolation elements with bilinear basis functions. The example calculations presented here that use these approximate boundary conditions are therefore accurate, but do not attain the maximum possible accuracy possible with the isogeometric formulation.

### 3.10 Time step size estimation

Since the cost of an explicit simulation is inversely proportional to the stable time step size, an accurate estimate of time step size is necessary for efficient simulations. The traditional approach to obtaining the time step size invokes two mathematical bounds on the maximum frequency of structural model. The first bound is the maximum frequency of the system is bounded from above by the maximum of the individual maximum frequencies of the elements,

$$\omega_{\max}^{\text{system}} \leq \max_{e=1, NEL} (\omega_{\max}^e). \quad (40)$$

A short proof is given in [26], where the original proofs were attributed to Irons [31] and Hughes *et al.* [28].

The second required bound is on the maximum frequency of the individual elements. The first bounds of this type were originally obtained for finite difference methods using linear basis functions in one dimension,

$$\frac{2}{\omega_{\max}^e} = \Delta t^e \leq \frac{\ell^e}{c_{\text{eff}}^e} \quad (41)$$

where  $\ell^e$  is the length of the element and  $c_{\text{eff}}^e$  is the effective sound speed (which is a function not only of the material properties but also the shock viscosity formulation [11]). Each constitutive model used in an explicit analysis therefore calculates effective elastic moduli in addition to updating the stress and internal history variables. This applies even to materials that may not have a classical elastic response, e.g., a viscous fluid. In two and three dimensions, the same expression is often used with a heuristic formula for a characteristic element length. A more rigorous bound [22] has been obtained in terms of the discrete gradient operator.

A more precise estimate of the maximum system frequency may be obtained using the power iteration method developed by Benson for multi-material arbitrary Lagrangian Eulerian (MMALE) methods [12]. Power iteration [42] obtains the maximum eigenvalue of the system by the iterative scheme

$$\left(\omega_{\max}^2 \Psi\right)^{i+1} = \mathbf{M}^{-1} \mathbf{K} \Psi^i \quad (42)$$

$$\left(\omega_{\max}^2\right)^{i+1} = \max_{n=1, \dots, NEQN} \left( \frac{\left(\omega_{\max}^2 \Psi\right)_n^{i+1}}{\Psi_n^i} \right) \quad (43)$$

where  $\mathbf{M}$  and  $\mathbf{K}$  are the mass and elastic stiffness matrices of the system,  $i$  is the iteration number,  $n$  is the equation number, and  $NEQN$  is the number of equations in the system. Twelve iterations are usually sufficient for convergence.

In practice, in an explicit code, the product  $\mathbf{K} \Psi$  is evaluated using the standard strategy of evaluating the internal force contribution on the element level from the strain calculated from the eigenvector and the effective elasticity matrix,  $\mathbf{C}$ , that is calculated from the same effective elastic moduli used in the sound speed calculation, namely,

$$\epsilon^\Psi = \mathbf{B} \Psi \quad (44)$$

$$\sigma^\Psi = \mathbf{C} \epsilon^\Psi \quad (45)$$

$$\mathbf{K} \Psi = \int \mathbf{B}^T \sigma^\Psi dx \quad (46)$$

and then the element contribution is assembled into the global vector. Note that boundary conditions, such as contact, that contribute terms to the stiffness matrix also contribute to the product  $\mathbf{K} \Psi$ .

The ratio,  $R$ , of the actual maximum system eigenvalue and the bound obtained from a traditional element characteristic length evaluation has been observed to change slowly with time even for problems involving large strains and material nonlinearities [12], allowing the actual maximum stable time step size to be safely approximated as

$$\Delta t_{\text{actual}} \approx R \Delta t^e. \quad (47)$$

where  $\Delta t^e$  is the traditional bound obtained by taking minimum time step size over all the elements. In practice, the ratio  $R$  is updated infrequently, with one power

iteration performed each time step, for a fixed small number of time steps in a larger time interval. The time interval between the updates of  $R$  depends on the particular problem; see Benson [12] for more details.

## 4 Numerical Examples

In this section we present one linear elastic and four nonlinear elastic-plastic computational examples. In all cases  $p + 1$  integration points in each in-plane direction between knots, and 3 integration points in the through-thickness direction are employed, where  $p$  is the polynomial order of the NURBS basis. We denote by  $E$ ,  $\nu$ ,  $\rho$ ,  $\sigma_y$ , and  $E_H$  the Young’s modulus, Poisson’s ratio, density, initial yield stress, and plastic hardening modulus, respectively.

### 4.1 Linear elastic benchmark example – Pinched cylinder

To assess the accuracy and convergence of the proposed approach, we solve a pinched cylinder linear elastic shell problem from the so-called “shell obstacle course” described in Belytschko *et al.* [10]. This problem was also solved using trivariate NURBS in [29] and, more recently, trivariate T-Splines in [3]. Note that the use of rational functions allows the exact representation of the problem geometry.

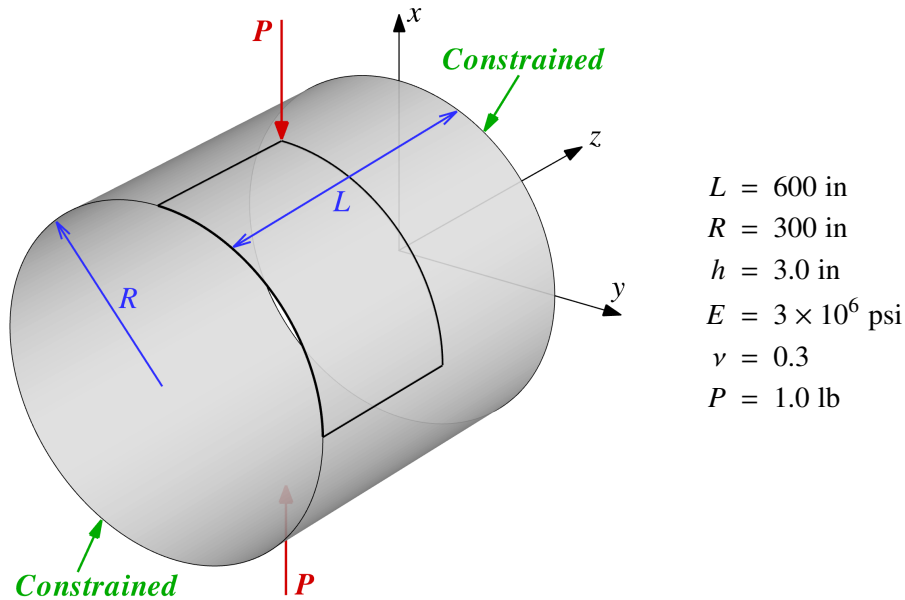


Fig. 2. Pinched cylinder: problem description. Cylinder is constrained at each end by a rigid diaphragm,  $u_x = u_y = \theta_z = 0$ .

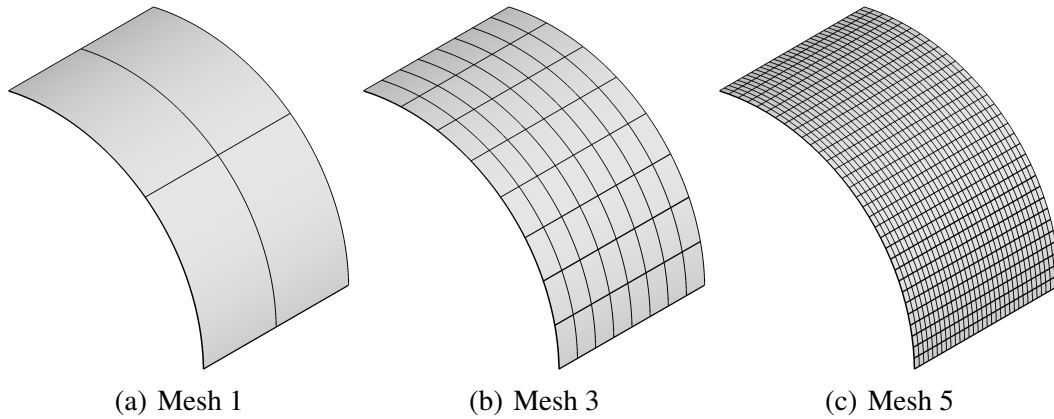


Fig. 3. Pinched cylinder: meshes.

The problem setup is illustrated in Figure 2. The loading consists of the application of inward directed point loads at the diametrically opposite locations on the cylinder surface. The displacement under the point load is the quantity of interest. A sequence of five meshes obtained by global  $h$ -refinement is used for this example. The first, third and fifth mesh from the sequence are shown in Figure 3. Quadratic through quintic NURBS are employed, with maximal continuity of the basis (i.e.,  $p - 1$ ) in each case. One eighth of the geometry is modeled with appropriate symmetry boundary conditions.

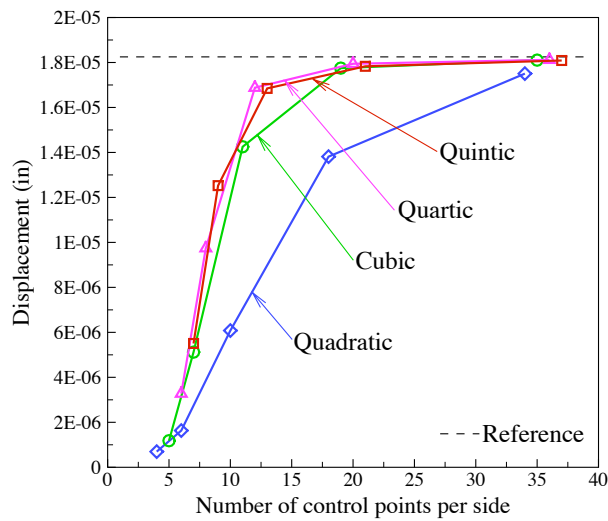


Fig. 4. Pinched cylinder: displacement convergence under the point load.

Displacement convergence under the point load is presented in Figure 4. The quadratic NURBS exhibit locking, which is gradually alleviated with the increasing order and continuity of NURBS. The results are consistent with those reported for volumetric NURBS [29] and T-Splines [3].

## 4.2 Nonlinear elasto-plastic examples

Conventional higher-order elements using Lagrangian interpolation are well known for their sensitivity to element distortion. To assess the robustness of the proposed elements in the presence of significant mesh distortion, a series of nonlinear shell example problems are solved. Improved performance of volumetric NURBS under severe mesh degeneration and distortion relative to standard finite element interpolations was noted in the recent work of Lipton *et al.* [33].

### 4.2.1 Plate loaded by pressure impulse

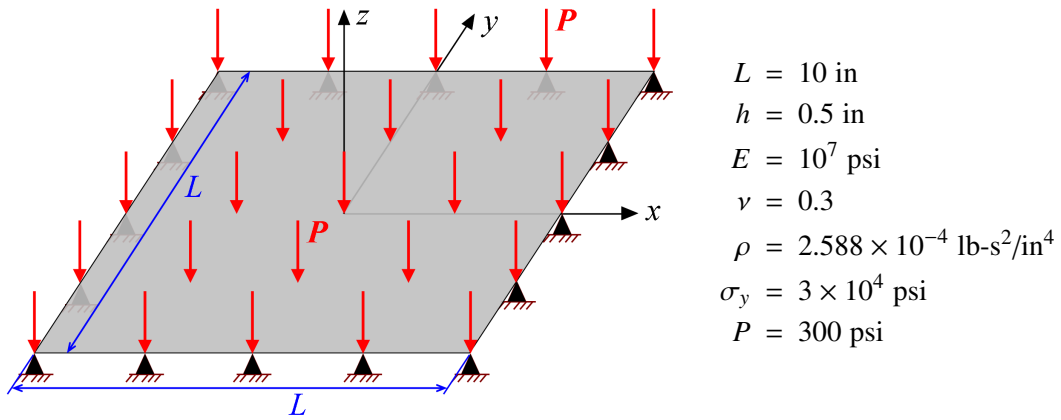


Fig. 5. Plate loaded by pressure impulse: problem description. All sides of the plate are simply supported.

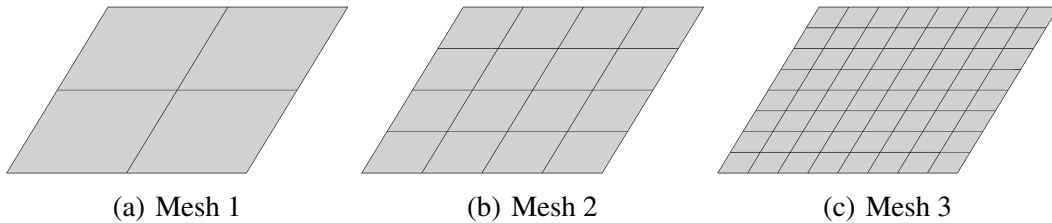


Fig. 6. Plate loaded by pressure impulse: meshes.

The problem setup is given in Figure 5. A simply supported plate is subjected to a uniform impulsively applied pressure load. An elastic-perfectly-plastic material is considered. Material parameters and problem dimensions are taken from Belytschko *et al.* [8] and are summarized in Figure 5. The full problem is modeled without symmetry assumptions in contrast to reference [8]. Meshes of  $2 \times 2$ ,  $4 \times 4$  and  $8 \times 8$  quadratic, cubic, and quartic NURBS elements are used in the computations and are shown in Figure 6. To emphasize that the locations of the control points are not in one-to-one correspondence with the domains of elements, the locations of the control points for a quartic element mesh are shown in Figure 7. Computational results employing a mesh of  $64 \times 64$  bi-linear Belytschko-Tsay shell elements are taken as the reference.

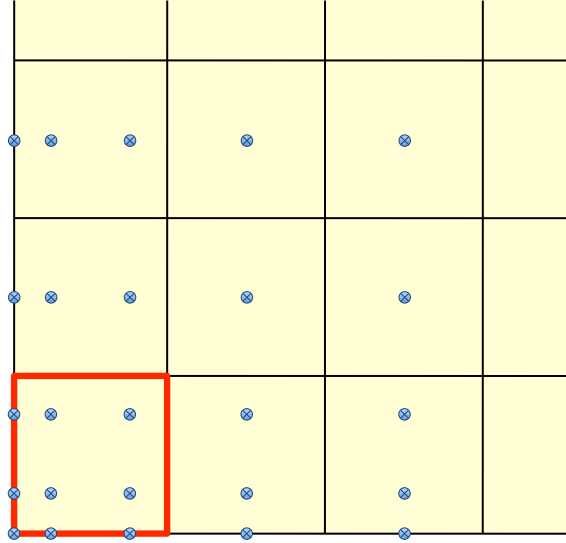


Fig. 7. One element in the quartic mesh and its associated control points.

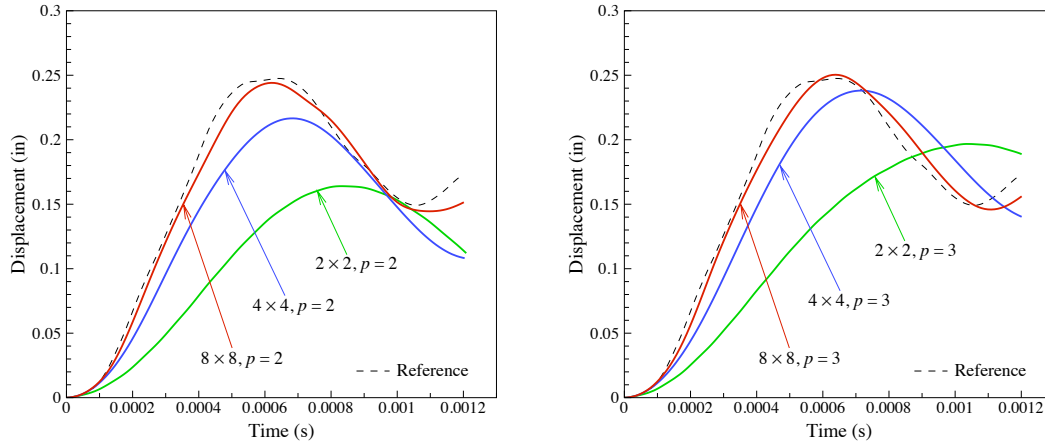
Figure 8 shows the time histories of the displacement of the center point of the plate for quadratic, cubic, and quartic NURBS. The finest mesh solutions closely approximate the reference result for all polynomial orders. Figure 8 also suggests that higher-order and higher-continuity NURBS perform better than their lower-order, lower-continuity counterparts on coarser meshes.

#### 4.2.2 *Roof loaded by velocity impulse*

The problem setup is given in Figure 9. This problem was also taken from [8] and consists of a  $120^\circ$  cylindrical panel loaded impulsively by specifying an initial velocity distribution. The problem dimensions and material data are summarized in Figure 9. An initial velocity normal to the shell surface is specified over a region marked on the figure.

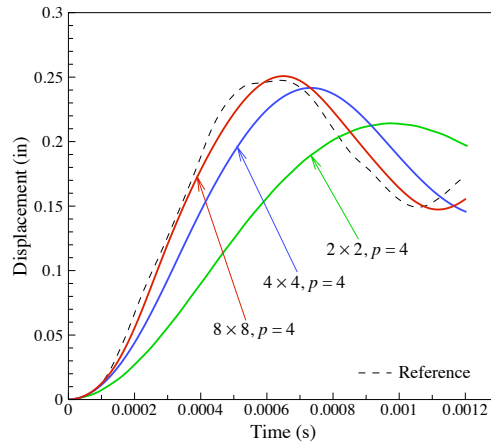
Quadratic, cubic, and quartic isogeometric elements are used in the calculations. The meshes are shown in Figure 10. Maximum continuity NURBS are used almost everywhere except along the parametric lines that define the region where the initial pulse is prescribed. Along these mesh lines the continuity of the NURBS basis is reduced to  $C^0$  so as to confine the impulse to the desired area. The normal velocity is specified on the control points by first extracting a consistent normal (see [23]) and then multiplying it with a prescribed velocity magnitude. The problem is solved on the entire domain with no symmetry assumptions.

Displacement histories of the point, initially located at  $x = 0$ ,  $y = 3$ , and  $z = 6$ , on each mesh are shown in Figure 11. Results are compared with the reference computations employing two meshes of 224 and 4512 Belytschko-Tsay elements, as well as experimental data from [34]. The quadratic NURBS solutions on the



(a)  $p = 2$

(b)  $p = 3$



(c)  $p = 4$

Fig. 8. Plate loaded by pressure impulse: center point displacement histories and convergence to the reference solution under  $h$ -refinement.

coarse mesh exhibit some locking, while on the fine meshes all the NURBS results are nearly identical to those using the finest Belytschko-Tsay mesh.

We attempted to solve the problem without isolating the impulse region with  $C^0$  lines on the same meshes as in Figure 10. In this case, the full continuity of the solution space is preserved. The initial conditions are imposed using the same definition of the control point normal as before. The initial velocity distributions and the comparison between the final roof shapes are given in Figure 12 (a) and (b). Due to the increased support of the fully continuous basis functions, the impulse discontinuity is smeared over a larger number of elements. It is also clear from the figure that the final shape of the roof in this case is significantly different from the expected result.

In order to obtain a better solution using a fully-continuous basis (i.e., no  $C^0$  lines),

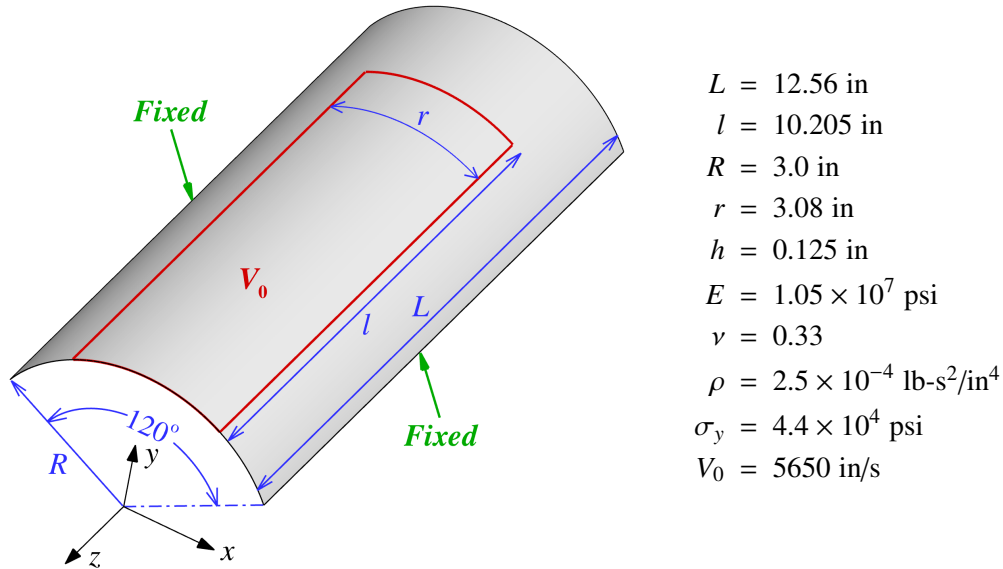


Fig. 9. Roof loaded by velocity impulse: problem description. The curved ends of the roof are hinged and the lateral boundaries are fixed.

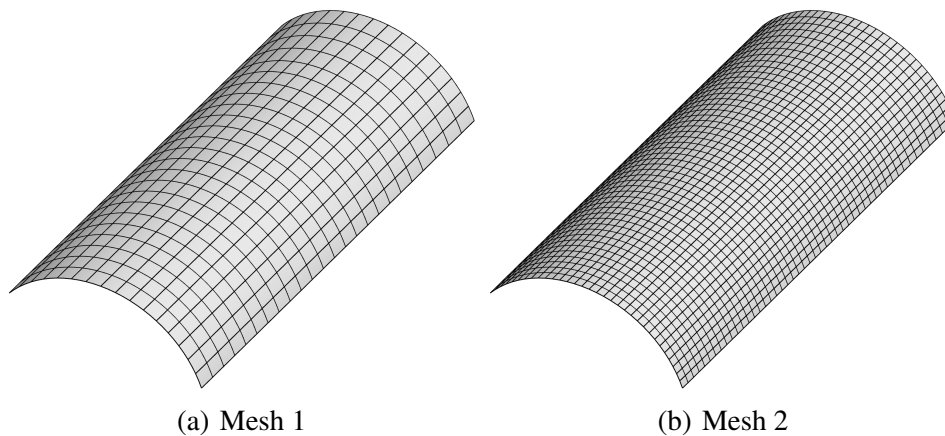


Fig. 10. Roof loaded by velocity impulse: meshes.

we constructed a new set of meshes, shown in Figure 13, in which we added small elements around the impulse region to reduce the spreading of the discontinuity. The initial velocity profile and the final shape are shown in Figure 12 (c). In this case, an improved response is obtained. The displacement history presented in Figure 14 is nearly identical to the  $C^0$  case.

This example demonstrates that in nonlinear shell analysis relatively small perturbation in the initial data may lead to drastically different results. One should keep this point in mind when designing automated procedures for going from design to analysis.

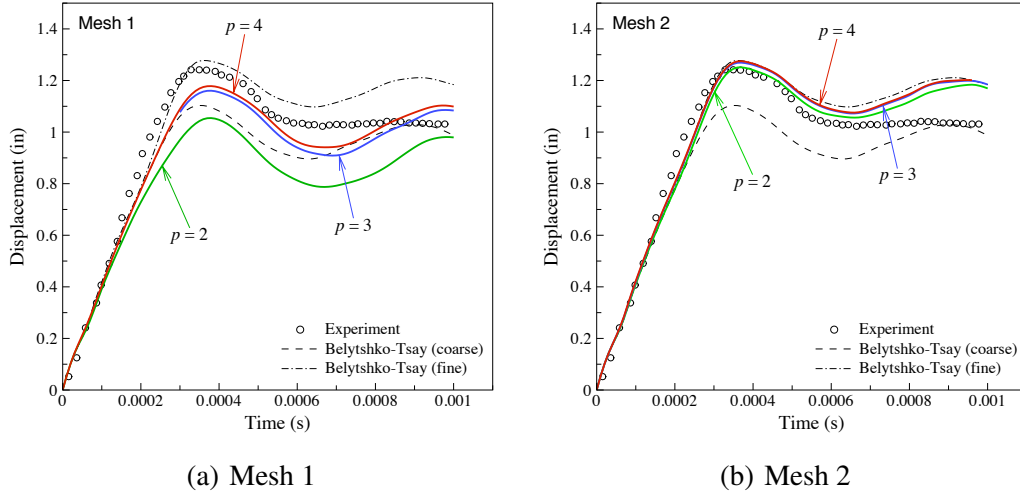


Fig. 11. Roof loaded by velocity impulse: displacement histories and convergence to the reference solution under  $k$ -refinement on meshes with  $C^0$  lines.

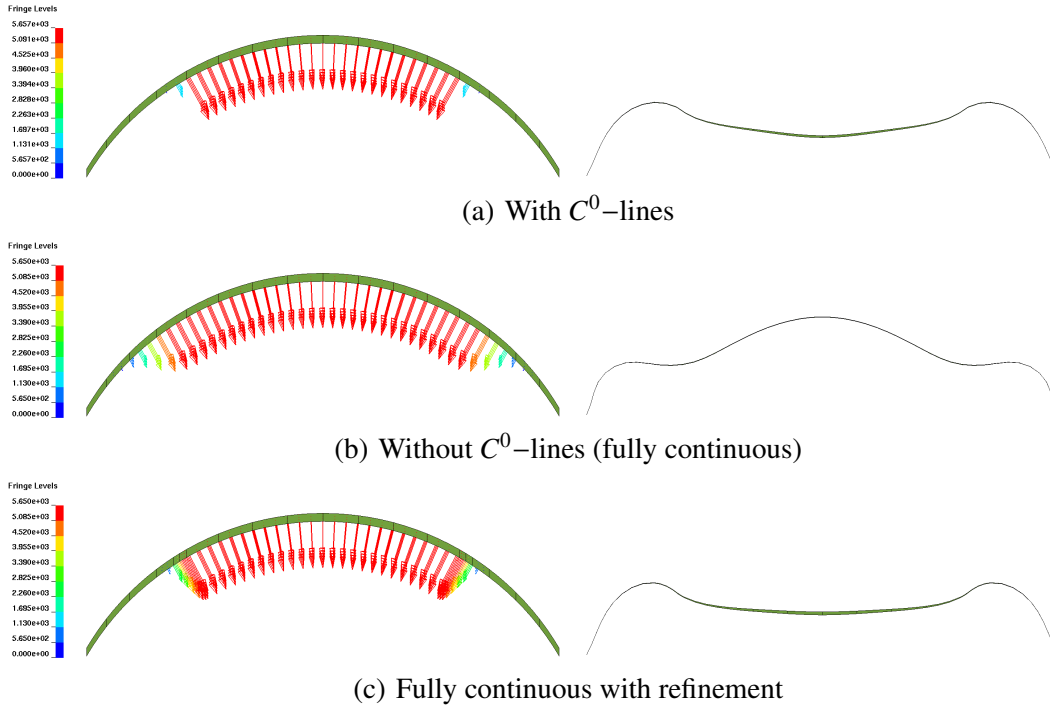


Fig. 12. The effect of the smoothness of the velocity boundary condition on the final results. Initial velocities (left) and final displacements (right) are taken from 1 row of elements of cubic mesh 1.

#### 4.2.3 Buckling of a cylindrical tube

This test case deals with nonlinear dynamic buckling of an imploded cylindrical tube. The problem geometry, boundary conditions, and material parameters are given in Figure 15. An isotropic elastic-plastic material with linear plastic hardening is used to model the material response. The problem is driven by an external

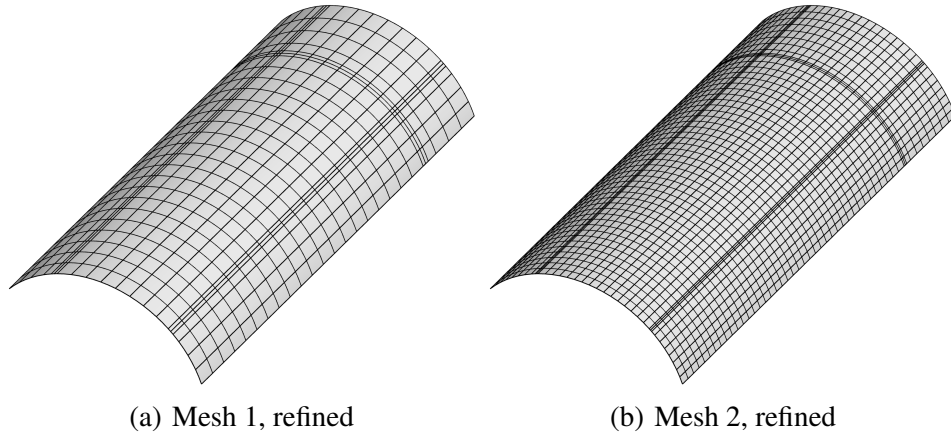


Fig. 13. Roof loaded by velocity impulse: refined meshes.

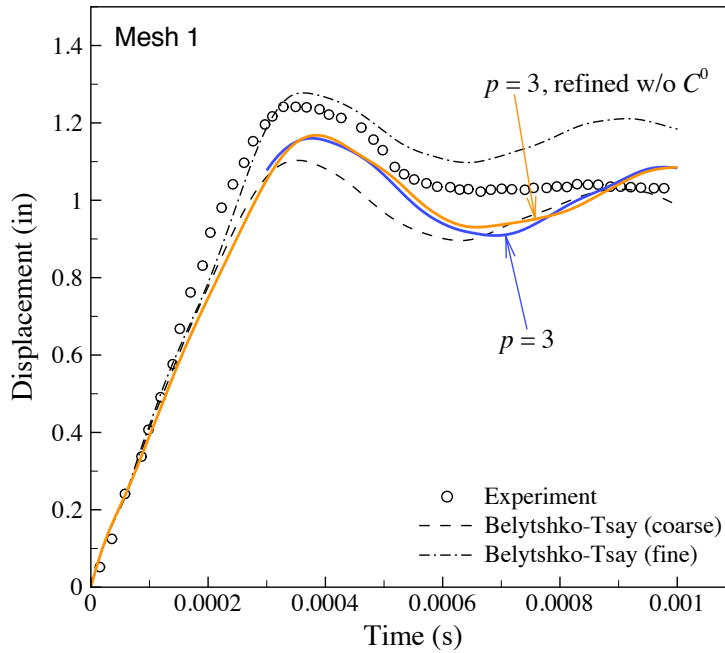


Fig. 14. Roof loaded by velocity impulse: displacement histories and convergence to the reference solution on cubic meshes without  $C^0$  lines. The  $C^0$  results are shown for comparison.

pressure. Quadratic, cubic, and quartic NURBS are used in the computations. The computational mesh consisting of 1440 NURBS elements is shown in Figure 16. The end zones with the sliding boundary conditions are isolated with  $C^0$  mesh lines from the rest of the cylindrical domain.

The experiment by Kyriakides and Lee [32] provides a test of how well the NURBS elements model dynamic buckling. The experimental results, which show the tube collapsed in its third buckling mode, are shown in Figure 17. An analytical solution [32] to the buckling problem predicts a pressure of 441.43 psi to initiate buckling

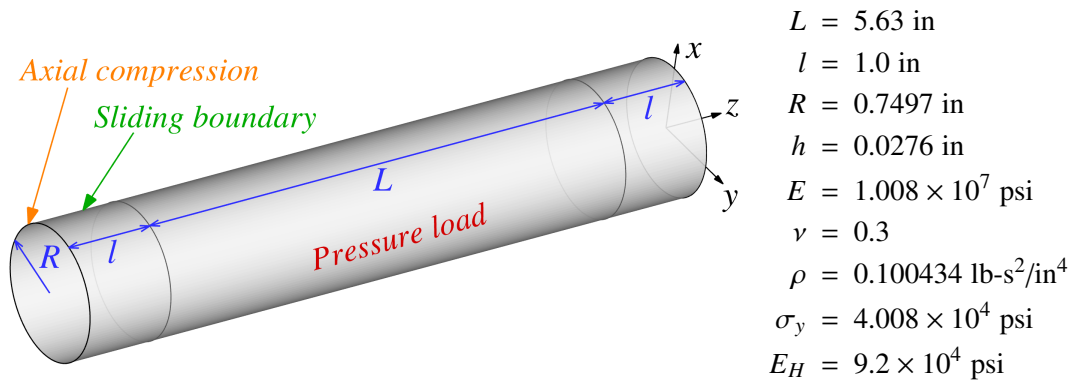


Fig. 15. Buckling of a cylindrical tube: problem setup.  $P$  is the pressure load. Sliding boundary conditions ( $u_x = u_y = 0, \theta_x = \theta_y = \theta_z = 0$ ) at the end zones and axial compression due to pressure ( $f_z = \frac{PR}{2}$ ) at the two edges are applied.

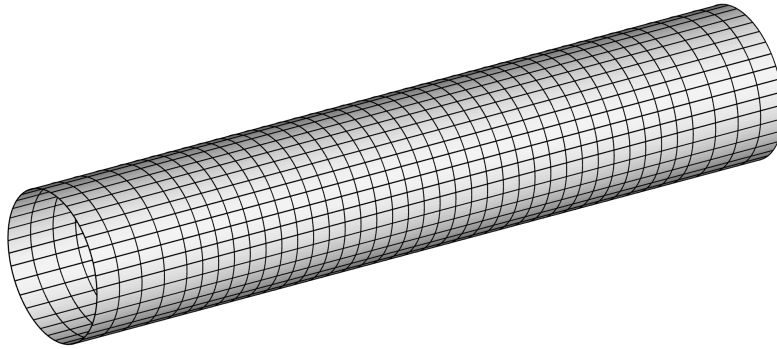


Fig. 16. Cylinder mesh

in the third mode, while the critical pressure in the experiment was found to be 410 psi.

Simulation results using 9210 Belytschko-Tsay elements in LS-DYNA are also used for comparison. In the calculations, in all cases, the pressure is linearly ramped up over a period of 1.0 ms and then held constant; the meshes are perturbed in the third mode by scaling the  $x$  and  $y$  coordinates of the control points by  $1 + \frac{1}{20} \cos(3\theta)$  [7]. We also note that no failure criterion is included in the calculations to model the fracture near the ends of the tube that is present in the experimental results.

The computational results are presented in Figures 18 and 19. The final shapes of the buckled tube are shown. The primary effect of elevating the degree and smoothness was a reduction in the pressure required for initiating buckling. Evidence of small amounts of shear locking in the quadratic elements is indicated by the 435 psi required to cause the buckling, while the cubic and quartic elements buckled at 405 psi. There was some variation in the maximum plastic strain on the mid-surface lamina, with the higher pressures giving slightly higher values for a fixed degree.

For example, the cubic solution had a maximum plastic strains of 0.266 at 435 psi and 0.214 at 405 psi, while the quartic solution had maxima of 0.252 and 0.241 at 435 and 405 psi, respectively. The reference solution with Belytschko-Tsay elements (see Figures 18 and 19) buckled at 410 psi, with a peak plastic strain of 0.226.



Fig. 17. Experimental results from Kyriakides and Lee [32]

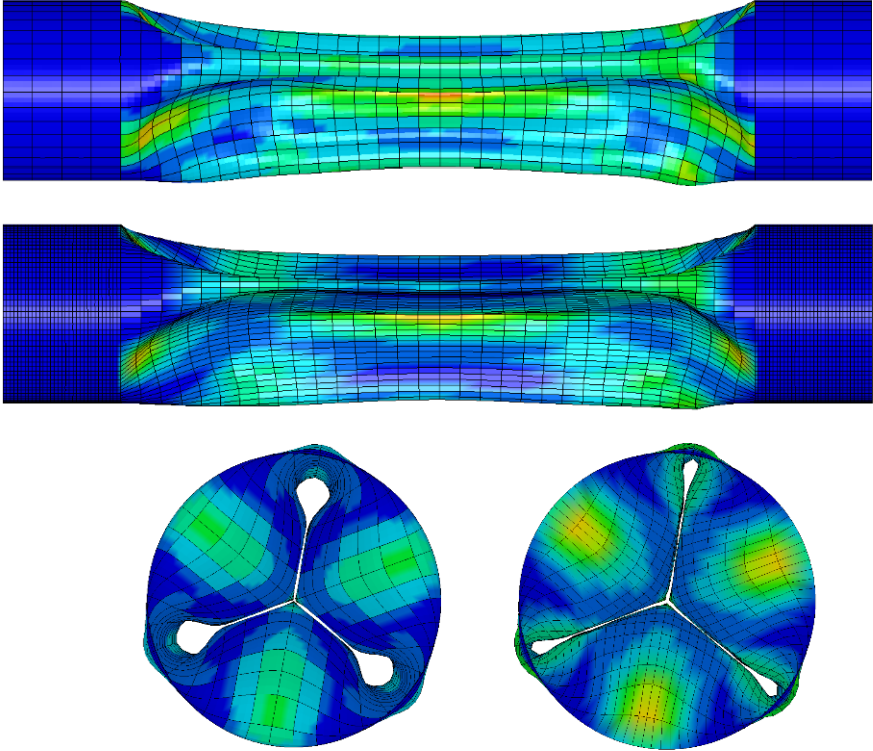


Fig. 18. Computational results using 1440 cubic NURBS elements and 9216 Belytschko-Tsay. Contours of plastic strain on the final configuration.

One interesting result noted in the computations that does not appear in the experiment is that the cylinder bounced back outward after the implosion, as indicated by the lobes near the axis, see Figure 19. There are many possible reasons for the discrepancy, ranging from the absence of modeling the fracture in the experiment to the choice of the surface stiffness used in the penalty contact, however the reason definitely appears to be independent of the underlying basis functions employed.

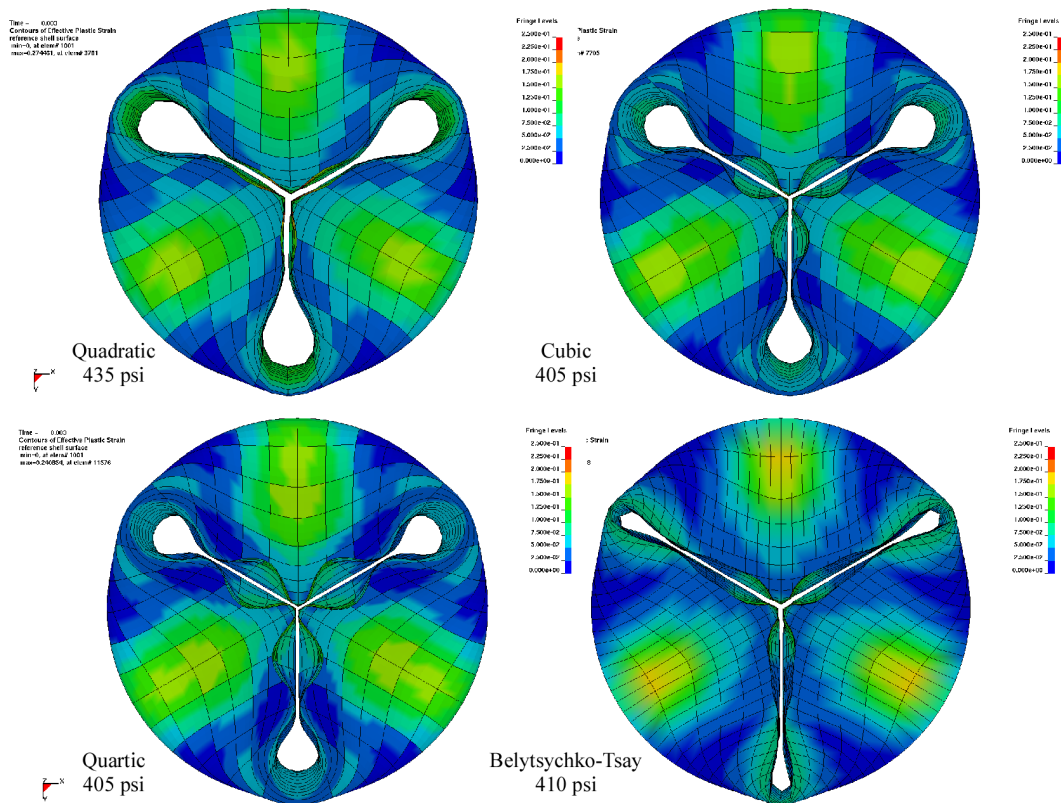


Fig. 19. Sectioned view of the buckled cylinders.

#### 4.2.4 Buckling of a square tube

The simulation of a square tube buckling into an accordion mode is a good test of the robustness of a shell element under large deformations. Originally solved as a demonstration of the single surface contact method [13] and now routinely used in automobile crashworthiness calculations, it remains a popular problem, even appearing on the cover of an excellent recent textbook [9].

The problem definition, geometry, material parameters and the NURBS mesh of the quarter of the domain are all given in Figure 20. An isotropic elastic-plastic material with linear plastic hardening is used to model the material response. The deformation is driven with a constant velocity at one end of the tube with the other end fixed. Quadratic and quartic NURBS meshes of 640 elements, and with 858 and 1156 control points, respectively, are used in the current simulations with symmetry boundary conditions. The standard single surface contact algorithm in LS-DYNA [13] is applied to the interpolation elements, where each quadratic and quartic isogeometric element is subdivided into 4 and 16 interpolation elements respectively.

A geometric imperfection with an amplitude of 0.05 mm, as shown in Figure 20, triggers the buckling at a height of 67.5 mm from the base. This imperfection is implemented by perturbing the initial coordinates of a mesh line of control points. Since the meshes are uniformly quadratic and quartic, the imperfections are slightly



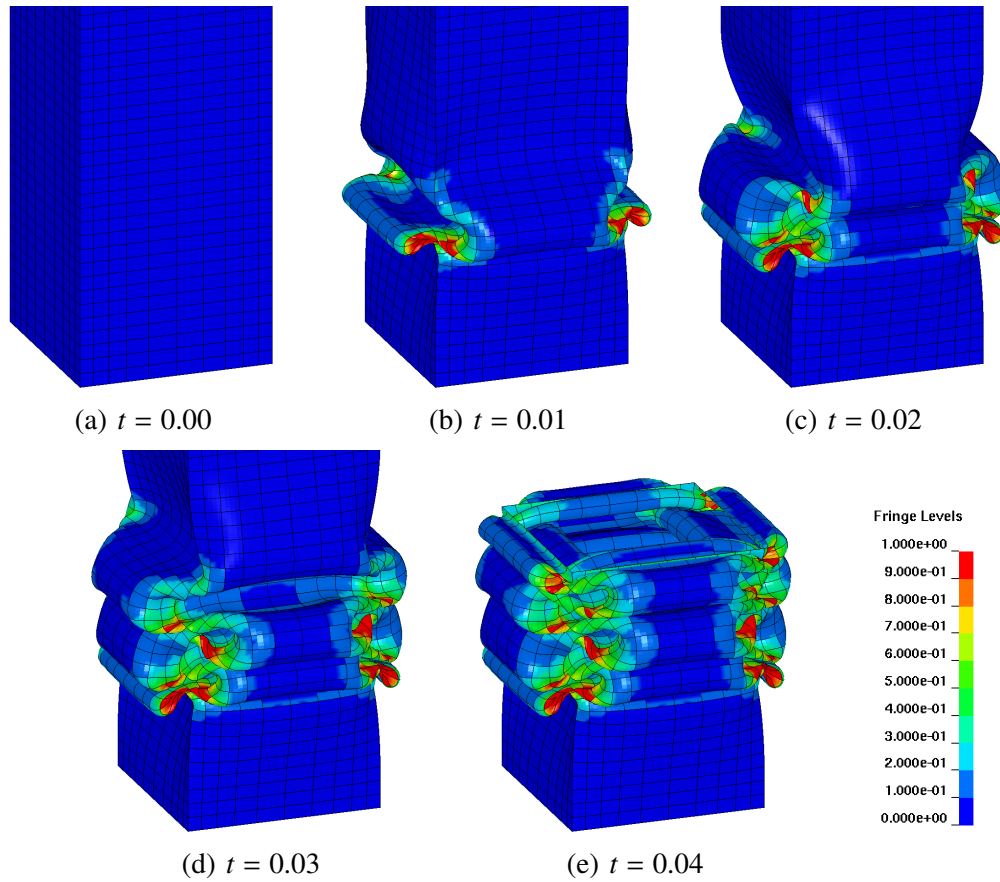


Fig. 21. A sequence of deformed shapes for the buckling of a square tube using quartic isogeometric elements.

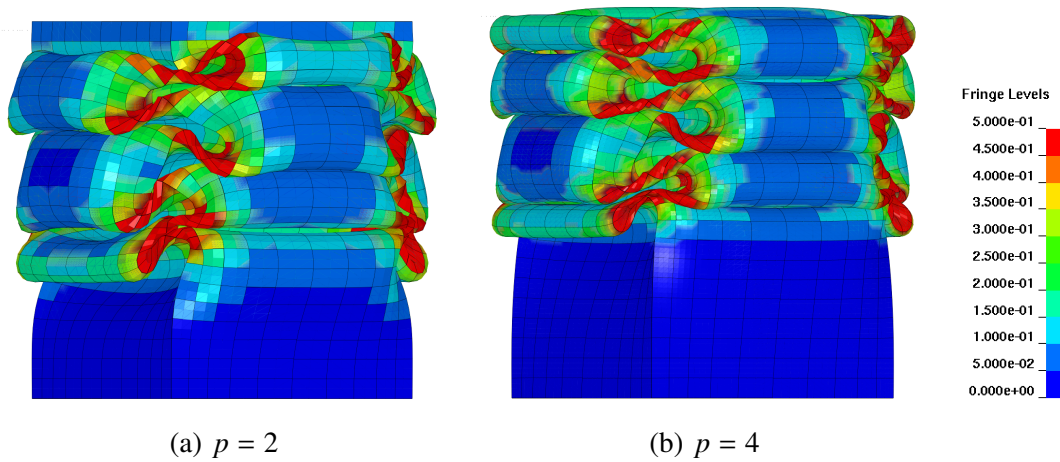


Fig. 22. The final deformed shapes for the quadratic (left) and quartic (right) shell elements solutions for the buckling of a square tube.

Based on the numerical results, the following conclusions are drawn:

- The isogeometric shell elements converge for the linear elastic shell problem as well as the isogeometric solid elements using quadratic displacements in the

thickness direction.

- There is a small amount of shear locking still present in the quadratic elements, but it almost entirely disappears in the cubic elements.
- The level of continuity maintained near discontinuities in the boundary conditions is an important analysis decision with a substantial effect on the accuracy of the solution.
- Higher order Lagrange element are notoriously sensitive to distortion. For example, the mid-side nodes of quadratic elements are sometimes deliberately positioned to model the singularity of a crack tip for linear fracture analysis [26]. This sensitivity to distortion prevents their use in many types of large deformation problems. In contrast, isogeometric elements using NURBS basis functions appear to be quite robust out to at least  $p = 4$ . In the study of Lipton et al. [33], it is noted that robustness of isogeometric NURBS elements *increases* with order. This robustness make them potentially attractive for many large deformation problems of industrial interest including sheet metal stamping and automobile crashworthiness.

## Acknowledgments

This research was supported by NSF grant 0700204 (Dr. Joycelyn S. Harrison, program officer) and ONR grant N00014-03-0236 (Dr. Luise Couchman, contract monitor).

## References

- [1] I. Akkerman, Y. Bazilevs, V.M. Calo, T.J.R. Hughes, and S. Hulshoff. The role of continuity in residual-based variational multiscale modeling of turbulence. *Computational Mechanics*, 41:371–378, 2008.
- [2] Y. Bazilevs, V.M. Calo, J.A. Cottrell, T.J.R. Hughes, A. Reali, and G. Scovazzi. Variational multiscale residual-based turbulence modeling for large eddy simulation of incompressible flows. *Computer Methods in Applied Mechanics and Engineering*, 197:173–201, 2007.
- [3] Y. Bazilevs, V.M. Calo, J.A. Cottrell, J.A. Evans, T.J.R. Hughes, S. Lipton, M.A. Scott, and T.W. Sederberg. Isogeometric analysis using T-splines. *Computer Methods in Applied Mechanics and Engineering*, 2008. Accepted for publication.
- [4] Y. Bazilevs, V.M. Calo, T.J.R. Hughes, and Y. Zhang. Isogeometric fluid-structure interaction: theory, algorithms, and computations. *Computational Mechanics*, 43:3–37, 2008.
- [5] Y. Bazilevs, V.M. Calo, Y. Zhang, and T.J.R. Hughes. Isogeometric fluid-

- structure interaction analysis with applications to arterial blood flow. *Computational Mechanics*, 38:310–322, 2006.
- [6] Y. Bazilevs and T.J.R. Hughes. NURBS-based isogeometric analysis for the computation of flows about rotating components. *Computational Mechanics*, 43:143–150, 2008.
- [7] T. Belytschko. Personal communication, 2008.
- [8] T. Belytschko, J. I. Lin, and C. S. Tsay. Explicit algorithms for the nonlinear dynamics of shells. *Computer Methods in Applied Mechanics and Engineering*, 42:225–251, 1984.
- [9] T. Belytschko, W. K. Liu, and B. Moran. *Nonlinear Finite Elements for Continua and Structures*. Wiley, West Sussex, England, 2001.
- [10] T. Belytschko, H. Stolarski, W. K. Liu, N. Carpenter, and J. S.-J. Ong. Stress projection for membrane and shear locking in shell finite elements. *Computer Methods in Applied Mechanics and Engineering*, 51:221–258, 1985.
- [11] D. J. Benson. Computational methods in Lagrangian and Eulerian hydrocodes. *Computer Methods in Applied Mechanics and Engineering*, 99:2356–394, 1992.
- [12] D. J. Benson. Stable time step estimation for multi-material Eulerian hydrocodes. *Computer Methods in Applied Mechanics and Engineering*, 167:191–205, 1998.
- [13] D. J. Benson and J. O. Hallquist. A single surface contact algorithm for the postbuckling analysis of shell structures. *Computer Methods in Applied Mechanics and Engineering*, 78:141–163, 1990.
- [14] M. Bischoff, W. A. Wall, K.-U. Bletzinger, and E. Ramm. Models and finite elements for thin-walled structures. In E. Stein, R. de Borst, and T. J. R. Hughes, editors, *Encyclopedia of Computational Mechanics, Vol. 2, Solids, Structures and Coupled Problems*, chapter 3. Wiley, 2004.
- [15] F. Cirak and M. Ortiz. Fully  $C^1$ -conforming subdivision elements for finite deformation thin shell analysis. *International Journal of Numerical Methods in Engineering*, 51:813–833, 2001.
- [16] F. Cirak, M. Ortiz, and P. Schröder. Subdivision surfaces: a new paradigm for thin shell analysis. *International Journal of Numerical Methods in Engineering*, 47:2039–2072, 2000.
- [17] F. Cirak, M. J. Scott, E. K. Antonsson, M. Ortiz, and P. Schröder. Integrated modeling, finite-element analysis, and engineering design for thin-shell structures using subdivision. *Computer-Aided Design*, 34:137–148, 2002.
- [18] E. Cohen, R.F. Riesenfeld, and G. Elber. *Geometric Modeling with Splines: An Introduction*. A K Peters, Natick, MA, 2001.
- [19] J.A. Cottrell, A. Reali, Y. Bazilevs, and T.J.R. Hughes. Isogeometric analysis of structural vibrations. *Computer Methods in Applied Mechanics and Engineering*, 195:5257–5297, 2006.
- [20] M.R. Dörfel, B. Jüttler, and B. Simeon. Adaptive isogeometric analysis by local  $h$ -refinement with T-splines. *Computer Methods in Applied Mechanics and Engineering*, 2008. Published online. doi:10.1016/j.cma.2008.07.012.
- [21] T. Elguedj, Y. Bazilevs, V.M. Calo, and T.J.R. Hughes.  $\bar{B}$  and  $\bar{F}$  projection

- methods for nearly incompressible linear and non-linear elasticity and plasticity using higher-order NURBS elements. *Computer Methods in Applied Mechanics and Engineering*, 197(33-40), 2008.
- [22] D. P. Flanagan and T. Belytschko. A uniform strain hexahedron and quadrilateral with orthogonal hourglass control. *International Journal for Numerical Methods in Engineering*, 17:679–706, 1981.
- [23] P. M. Gresho and R. L. Sani. *Incompressible Flow and the Finite Element Method*. Wiley, New York, NY, 1998.
- [24] J. O. Hallquist. LS-DYNA theoretical manual. Technical report, Livermore Software Technology Corporation, 1998.
- [25] K. Höllig. *Finite Element Methods with B-Splines*. SIAM, Philadelphia, 2003.
- [26] T. J. R. Hughes. *The Finite Element Method, Linear Static and Dynamic Finite Element Analysis*. Dover, 2000.
- [27] T. J. R. Hughes and W.K. Liu. Nonlinear finite element analysis of shells: Part I. Three-dimensional shells. *Computer Methods in Applied Mechanics and Engineering*, 26:331–362, 1981.
- [28] T. J. R. Hughes, K. S. Pister, and R. L. Taylor. Implicit-explicit finite elements in nonlinear transient analysis. *Computer Methods in Applied Mechanics and Engineering*, 17/18:159–182, 1979.
- [29] T.J.R. Hughes, J.A. Cottrell, and Y. Bazilevs. Isogeometric analysis: CAD, finite elements, NURBS, exact geometry, and mesh refinement. *Computer Methods in Applied Mechanics and Engineering*, 194:4135–4195, 2005.
- [30] T.J.R. Hughes, A. Reali, and G. Sangalli. Duality and unified analysis of discrete approximations in structural dynamics and wave propagation: Comparison of  $p$ -method finite elements with  $k$ -method nurbs. *Computer Methods in Applied Mechanics and Engineering*, 197:4104–4124, 2008.
- [31] B. M. Irons. Applications of a theorem on eigenvalues to finite element problems. Technical Report CR/132/70, University of Wales, Department of Civil Engineering, Swansea, U. K., 1970.
- [32] S. Kyriakides. Personal communication, 2008.
- [33] S. Lipton, J.A. Evans, Y. Bazilevs, T. Elguedj, and T.J.R. Hughes. Robustness of isogeometric structural discretizations under severe mesh distortion. *Computer Methods in Applied Mechanics and Engineering*, 2008. Accepted for publication.
- [34] L. Morino, J.W. Leech, and E.A. Wittmer. An improved numerical calculation technique for large elastic-plastic transient deformations of thin shells: Part 2 – Evaluation and applications. *Journal of Applied Mechanics*, pages 429–435, 1971.
- [35] L. Piegl and W. Tiller. *The NURBS Book (Monographs in Visual Communication)*, 2nd ed. Springer-Verlag, New York, 1997.
- [36] D.F. Rogers. *An Introduction to NURBS With Historical Perspective*. Academic Press, San Diego, CA, 2001.
- [37] S. Schoenfeld and D. J. Benson. Quickly convergent integraton methods for plane stress plasticity. *Communications in Applied Numerical Methods*, 9:293–305, 1993.

- [38] T.W. Sederberg, G.T. Finnigan, X. Li, H. Lin, and H. Ipson. Watertight trimmed NURBS. *ACM Transactions on Graphics*, 27 (3), 2008.
- [39] J. C. Simo and T. J. R. Hughes. *Computational Inelasticity*. Springer, New York, 2000.
- [40] W. A. Wall, M. A. Frenzel, and C. Cyron. Isogeometric structural shape optimization. *Computer Methods in Applied Mechanics and Engineering*, 197:2976–2988, 2008.
- [41] H. Wang, Y. He, X. Li, X. Gu, and H. Qin. Polycube splines. *Computer-Aided Design*, 40:721–733, 2008.
- [42] J. H. Wilkinson. *The Algebraic Eigenvalue Problem*. Oxford University Press, 1965.